Activated carbons with high nitrogen content by a combination of hydrothermal carbonization with activation

C. Laginhas[1], J. M. Valente Nabais[1*], M. M. Titirici[2,3]

[1]*Departamento de Química, Escola de Ciências e Tecnologia, Centro que Química de Évora, Instituto de Investigação e Formação Avançada, Universidade de Évora, Rua Romão Ramalho 59, 7000-671 Évora, Portugal*
[2]*Queen Mary University of London, School of Materials Science & Engineering, E14NS Mile End Road, London, UK*
3 Materials Research Institute, Queen Mary University of London, E14NS, Mile End Road, London, UK

Abstract

This paper reports the production of carbons materials with a nitrogen content around 8% (w/w) and a well-developed porous structure, with BET surface area and pore volume up to $2130 m^2 g^{-1}$ and $1,12 cm^3 g^{-1}$, respectively, produced by a combination of hydrothermal carbonization, an environmental friendly method in the production of sustainable tunable carbon materials, with traditional activation methods. The porosity was developed through an activation process according to different routes, namely activation with CO_2 and chemical activation using $CaCO_3$ and K_2CO_3. The successful production of activated carbons using chitosan as a nitrogen source revealed to be a good alternative to post-synthesis methods.

Keywords: Activated carbons, hydrothermal carbonization, chitosan, activation.

* Corresponding author. Tel: (+351) 266 745318. E-mail: jvn@uevora.pt (João Nabais)

1. Introduction

Carbon materials have been extensively studied during the last century, especially after the discovery of fullerenes [1] and carbon nanotubes [2], because of their versatility and wide range of applications, such as carbon sequestration [3], pollutants removal [4-7], gas storage [8], carbon fuel cells [9, 10] and cell biology [11]. Among all carbon materials, activated carbons (AC) are probably the most well-known and broadly used class of materials. This is due to several factors including the possibility to prepare AC in different formats such as powder [12, 13], granular [14], monoliths [15] or, more recently, materials with spherical morphology [16]. Also, ACs usually has a high wear resistance, good mechanical strength, good adsorption capacity and low ash content. The spherical ACs have a more regular and smoother surface and a higher control over the pore size distribution [17, 18].

The hydrothermal carbonization (HTC) is a thermochemical process used to produce a coal-like product (C~40-50 wt%) from an aqueous suspension of raw biomass or carbohydrates using an autoclave under moderate temperatures (180-250ºC) and self-generated pressures. The resulting carbons have a regular morphology and a rich surface chemistry. HTC presents some advantages in comparison with classical pyrolysis, regarding its simplicity, low cost production, and energy and CO_2 efficiency. It can be classified as a "green" process since it takes place without the use of organic solvents, surfactants or catalysts, uses moderate temperatures and has minimum CO_2 emissions [16].

The conversion mechanism of biomass/carbohydrates into carbon via hydrothermal carbonization involves hydrolysis of cellulose/hemicellulose into smaller molecules such as hydroxymethylfurfural and levulinic acid, which can undergo further condensation into brunched furan-based aromatic compounds [19]. The dehydration and decarboxylation reactions are promoted by the presence of water under subcritical regime [20-22]. It is also possible to add different chemicals to promote specific chemical functionalization of the surface [23].

Many precursors have been studied over the last few years, from simple sugars like glucose to more complex ones such as starch or cellulose. Among the various classes of carbon materials nitrogen doped materials presents themselves as one of the most promising ones because of the special properties induced by nitrogen doped within the carbon matrix [17].

Chitosan is an aminopolysaccharide biopolymer, resulting from the deacetylation of chitin, with a complex structure and highly sophisticated functions. Because of its remarkable biocompatibility, low toxicity and biodegradability, it is considered a green option for the production of nitrogen doped carbon materials. Chitosan is abundant, cheap and easily accessible with a wide range of applications, from biomedical to industrial areas.

Some recent publications have reported the production of activated carbons using the HTC process first as a route to improve the porosity of these materials, preserving at the same time the spherical morphology of the particles. Recently Wenming Hao et al successfully produced activated carbons from HTC carbonized waste using physical and chemical activation, with surface areas greater than $500m^2g^{-1}$ [24, 25].

The aim of this work is to investigate the production of hydrothermal carbons from chitosan, through different experimental conditions, and subsequent activation process through physical activation with CO_2 and chemical activation with $CaCO_3$ and K_2CO_3 in order to achieve functionalized carbons with tunable properties.

2. Experimental

2.1 Materials

The precursor, cithosan, with molecular weight between 100000 and 300000, supplied by Acros Organics, was used as received.

2.2 Methods

2.2.1 Carbon synthesis by hydrothermal carbonization

The HTC samples were produced via a systematic approach based on the experimental factorial design using temperature and time as variables. The water/precursor ratio (v/w) was fixed during the experiments at 1:6; the temperature tested was 180, 190 and 200ºC, and the time 8, 12 and 24h, corresponding to the levels -1, 0 and +1 of the experimental design, respectively.

The precursor was mixed with water and stirred for 1h in a glass vessel at 25ºC, then transferred to a Teflon-lined autoclave and heated in an oven at the desired temperature. The autoclave was cooled down to room temperature and the solid material was then filtered, washed with distilled water followed by Soxhlet extraction with ethanol (Panreac, 96% v/v PA) during 24h. The carbon material was oven dried at 100ºC for 24h.

Each synthesized material was named Q followed by the synthesis specifications, namely temperature (180, 190 or 200) and time of carbonization. For example, the sample Q200-24 represents a HC produced from chitosan at 200ºC during 24h.

2.2.2 Activation Process

Sample Q200-24 was activated under a CO_2 flow of 85mL/min at 800ºC for 1, 3 and 5 hours using a tubular horizontal furnace. In a separate experiment, the carbonized sample was also activated by impregnation with a saturated $CaCO_3$ or K_2CO_3 solution, for 6h according to the ratio of 1:10 w/v, followed by pyrolysis in a tubular horizontal furnace under N_2 flow (85mL/min) at 800ºC during 1, 3 and 5 hours. The samples were washed with distilled water for 24h and oven dried at 100ºC for another 24h.

The activated samples were identified by including after the letter A, which stands for activated sample, the designation C, Ca and K, respectively for samples activated with CO_2, $CaCO_3$ and K_2CO_3, followed by the time of activation 1,3 or 5. As example AC-3

represents the sample produced by activation of Q200-24 by carbon dioxide for 3 hours at 800ºC.

Selected samples were oxidized with concentrated nitric acid (HNO_3) by mixing 1g of carbon with 50mL of acid. The mixture was heated up to 90ºC under mild agitation during 1h. The sample was then filtered and washed with distilled water and oven dried at 100ºC for 24h. The oxidized samples were named according to the original activated samples followed by the letters Ox.

2.3 Samples characterization

The nitrogen adsorption/desorption isotherms at 77K were carried out in an Autosorb iQ, Quantachrome Instruments. The samples were initially degassed at 300ºC during 4h at a stepwise of 1ºC/min, under ultra-vacuum.

The morphology of the samples was examined by Scanning Electron Microscopy (SEM) using a HITACHI 3700N microscope.

The chemical composition and functionalities of samples were evaluated by infrared spectroscopy (FTIR) and elemental analysis. The FTIR spectra were obtained with a Perkin Elmer, model Spectrum Two spectrophotometer, according to the KBr disc method, with a resolution of $4cm^{-1}$ and 20 scans. The elemental analysis (C, H, N, S and O) was done in a Eurovector Euro EA, samples were weighted in a Sartorius micro pro 11 ultra-precision balance.

The point of zero charge was determined by mass titration, details described elsewhere [26].

3. Results and Discussion

3.1 Characterization of the precursors and hydrothermal carbons

As can be seen in table 1, the precursor has a naturally high content in nitrogen, which can be considered an advantage for specific applications. We can also observe that chitosan presents carbon and oxygen contents typical of carbon materials precursors, indicating its suitability for the production of these materials.

Table 1. Elemental analysis of the precursor

Precursor	Elemental Analysis / %(w/w)					
	C	N	H	S	O	Undetermined[a)]
Chitosan	40.38	7.72	7.81	<d.l.	33.70	10.39

a - by difference; d.l. – detection limit

The thermal decomposition under a flow of nitrogen of the precursor and Q200-24 was monitored by thermogravimetry as shown in figure 1. As can be seen in fig. 1, chitosan showed two thermal degradation processes. The first one centered at 76ºC, as indicated on the dTG curve, is related to loss of adsorbed water and represents less than 10% weight lost. It is also noteworthy to mention this process goes up to 140ºC due to the hydrogen bonding between polymer chains and water molecules. The second thermal degradation process, centered at 316ºC, corresponds to 48% weight loss and can be attributed to polymer degradation and chitosan deacetylation. At 700ºC the material loose about 60%, thus chitosan can be considered thermally more stable than other precursors such as coffee endocarp, esparto grass or vine shoot [27-29]. The sample Q2006-24 showed a significantly lower weight lost when compared with chitosan, but the same decomposition pattern with the presence of two main weight lost events. The first one, also around 76ºC, have a lower extent than chitosan with only ~3% of weight lost. The second one around 416ºC with a weight loss of 32% corresponding to the release of volatile species namely oxygenated functional groups [30].
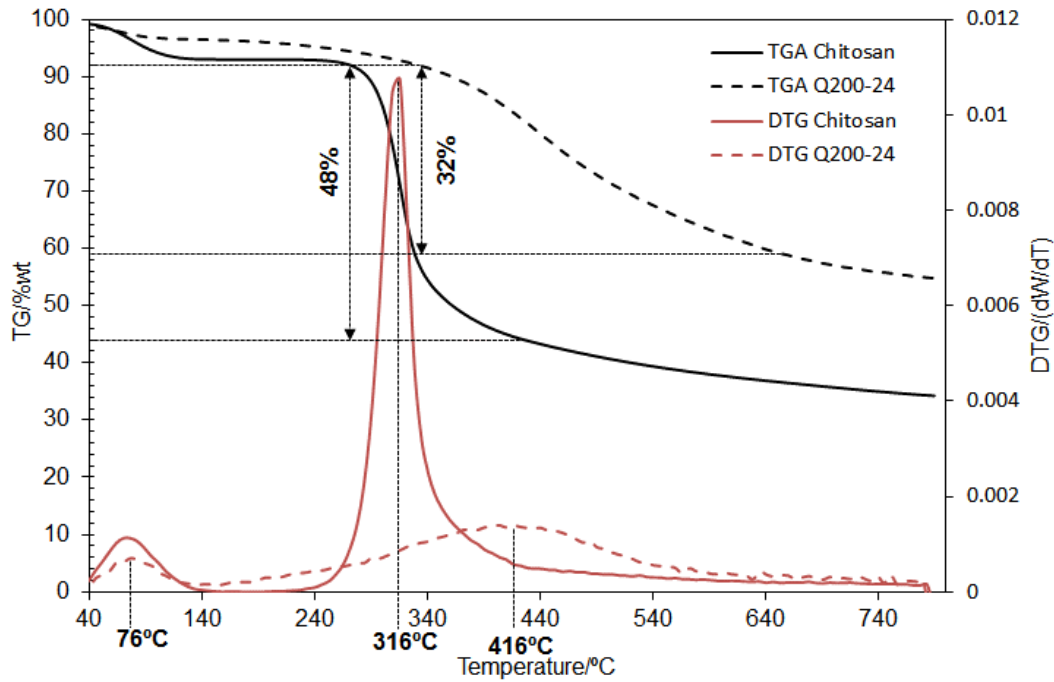
Figure 1. TGA and DTG curves of chitosan and Q200-24

The morphological analysis done by SEM, shown in figure 2, revealed that sample Q2006-24 proved to have mix morphology with regions composed by sphere-like structures and others very similar to the chitosan structure. This can be attributed to the thermal stability of chitosan that can lead to higher resistance to the hydrocarbonisation method with only a partial degradation of the original structure. The presence of spherical-like structures in the carbonized samples are characteristic of the hydrothermal process, as already reported by Titirici et al., Marta Sevilla et al. and S. Román et al. [31-35].
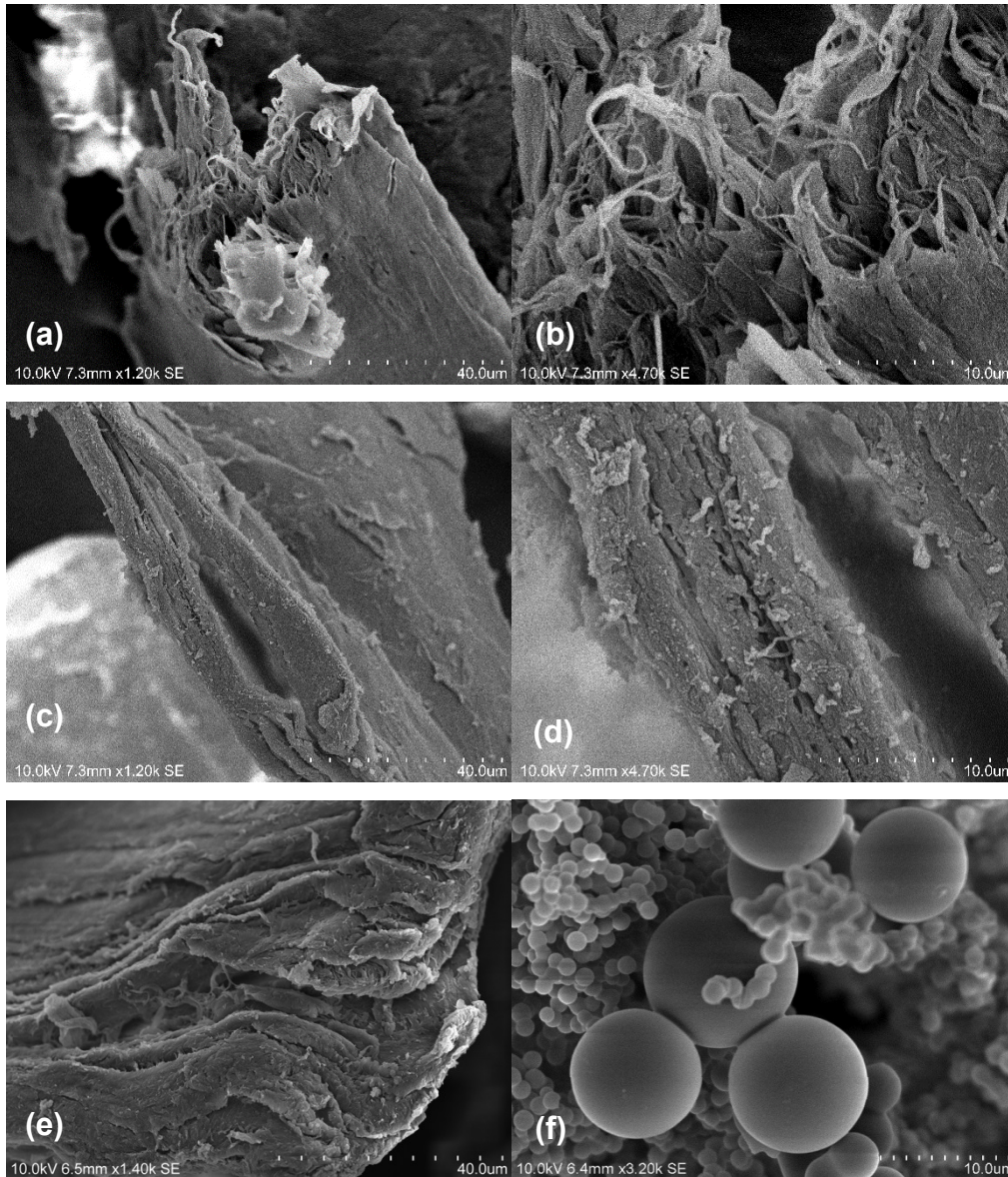
Figure 2. SEM images of Q200-8 ((a) and (b)), Q200-12 ((c) and (d)) and Q200-24 ((e) and (f)).

The elemental composition of the hydrocarbons (HTC), presented in Table 2, shows that all samples have a carbon content within the range ~40 to 60%(w/w), as expected for a carbonaceous material. We can observe an increase of the carbon content with the increase of the temperature or time at which the hydrothermal carbonization is done.

It is worthwhile to note the relatively high nitrogen content between 7.66 and 10.07% (w/w), which proves that the hydrocarbonisation process lead to a fixation of nitrogen into the structure of the HTC. This fact is relevant for potential applications of the materials, such as carbon dioxide capture, electrodes in supercapacitors. The oxygen

content decreases with carbonization from 44 to 29-16% (w/w), following the same path, decrease with carbonization temperature and time.

The point of zero charge can be observed in Table 2. All samples have acidic properties with values always less than 7. A slight increase in the point of zero charge with the carbonization time or temperature is observed.

Table 2. Elemental analysis and point of zero charge of the hydrothermal carbons

Sample	pH_{pzc}	Elemental Analysis / %(w/w)				Undetermined (%w/w)[a]
		C	N	H	O	
Q180-8	5.77	40.93	7.68	16.38	28.02	6.99
Q180-12	5.81	42.00	7.66	15.89	27.24	7.21
Q180-24	5.82	45.15	8.21	9.95	27.05	9.64
Q190-8	5.79	37.46	7.70	14.81	29.50	10.53
Q190-12	5.85	43.58	7.80	13.36	25.76	9.50
Q190-24	5.98	55.11	9.41	8.68	21.47	5.33
Q200-8	5.85	48.65	8.28	12.37	25.05	5.65
Q200-12	5.89	54.67	9.19	10.96	19.08	6.10
Q200-24	6.01	59.62	10.07	4.97	16.42	8.92

a) by difference

The hydrothermal carbonization was optimized to produce chars with the highest carbon and nitrogen content. The systematic approach used on this work gives us the possibility of plot the results in the format of a surface graph representing the response in terms of the carbon and nitrogen content according the time and temperature of carbonization, shown in Fig. 3. The fitting of the experimental data was done with the Kriging method and a polynomial function of the type

$$Mp = \alpha_1 X_{1i} + \alpha_2 X_{2i} + \alpha_3 X^2_{1i} + \alpha_4 X_{1i}X_{2i} + \alpha_5 X^2_{2i}$$

It is possible to observe in Figure 3 that the best experimental conditions to produce the hydrocarbons with the highest content of nitrogen and carbon are a temperature of

200ºC for 24h. In consequence, sample Q200-24 was selected to be used on the subsequent activation experiments.
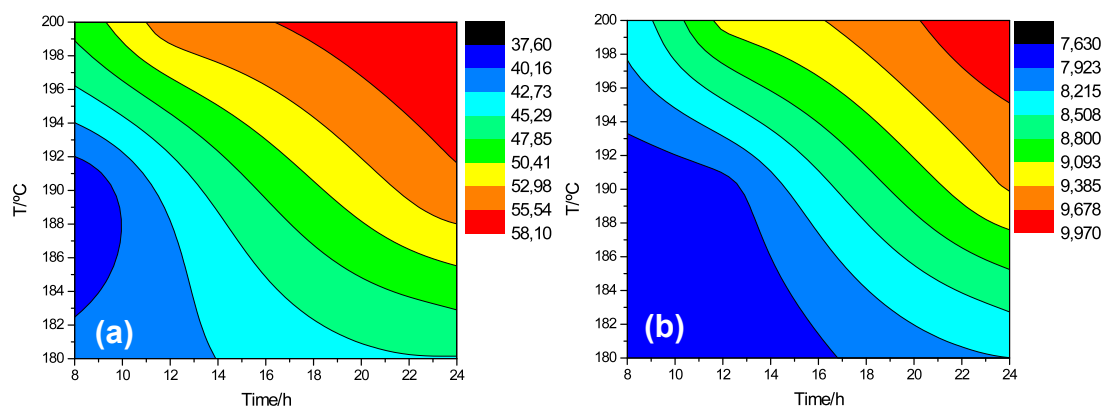

Figure 3. Carbon (a) and nitrogen (b) content in HTC samples.

The changes in the functional groups and chemical structure from the precursor to the hydrothermal carbons were studied by FTIR. Figure 4 shows the chitosan spectra and representatives HTC samples. Chitosan spectrum shows two different alcohol group conformations, the first one with a broad band at 3372, 1323 and 1091cm^{-1} related to the stretching vibration of hydroxyl group, deformation of OH group and stretching vibration of C-O bond, respectively. The second conformation has also the OH stretching vibration at 3372cm^{-1}, the OH deformation at 1418cm^{-1} and the C-O bond stretching at 1033cm^{-1}. The high intensity broad band at 3372cm^{-1} can hide two sharp bands, located at 3408 and 3372cm^{-1}, related to NH antisymmetric and symmetric stretching vibration, respectively. The band at 1600cm^{-1} can be related to deformation of NH$_2$ and at 1323cm^{-1} to the stretching of C-N bond. Ether groups were also found through identification of characteristic stretching vibration of C-O-C at 1252cm^{-1} and 1091cm^{-1} (antisymmetric) and 1033cm^{-1} (symmetric). It was also possible to identify the presence of aliphatic structures characterized by C-H symmetric stretching at 2940cm^{-1} and C-H deformation at 1477cm^{-1}. The band located at 1621cm^{-1}, visible for Q200, can be related to different groups, in particular to C=N stretching vibration or to C=O stretching vibration in amides. It was also possible to identify some bands that may be related to stretching of aromatic ring located at 1621, 1490 and 1437cm^{-1} as well as deformation of C-H at 891cm^{-1}.

There are some key bands that tend to fade with temperature. The band at 1653cm^{-1}, related to C=O stretching in amides and C=C stretching vibration of alkenes, well defined in chitosan, has almost vanished on the HTCs. Other difference is the band at 1380cm^{-1}, related to OH deformation in alcohol and CH symmetric deformation in alkanes, which is not present in HTC produced at 180ºC and 190ºC but reappears for HC produced at 200ºC. The band at 1252cm^{-1}, which can be attributed to strong C-O stretching vibration, C-C skeletal, C-N and N-H stretching and bending in amides, respectively, C-H in plane bending and to C-O-C symmetric stretching in ethers, also evolves from the precursor to Q200-24. The same behavior can be seen in C-O stretching vibration in alcohols at 1158cm^{-1}as well as the band in 895cm^{-1}, related to C-H deformation and O-H out-of-plane deformation.
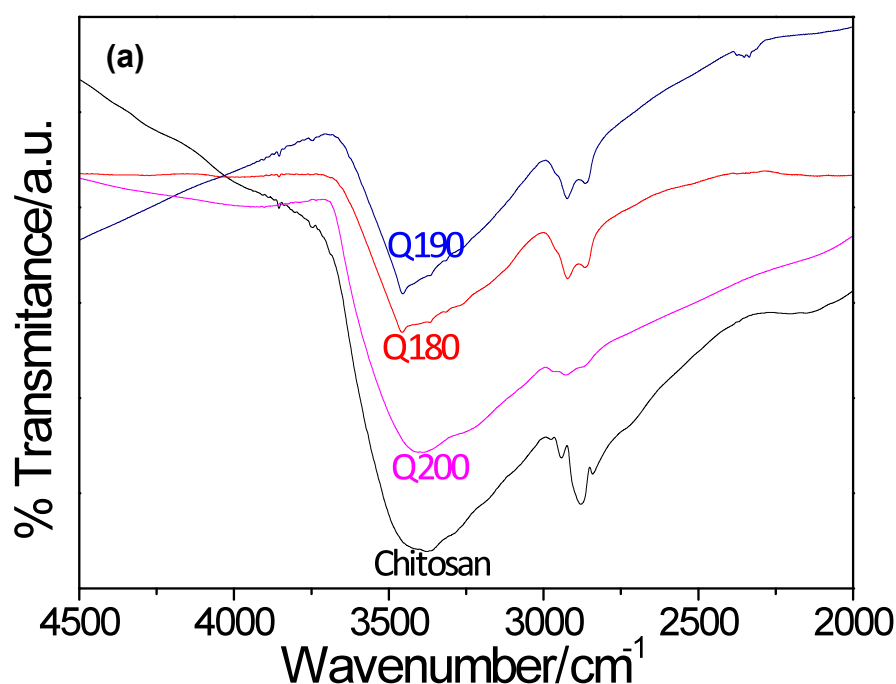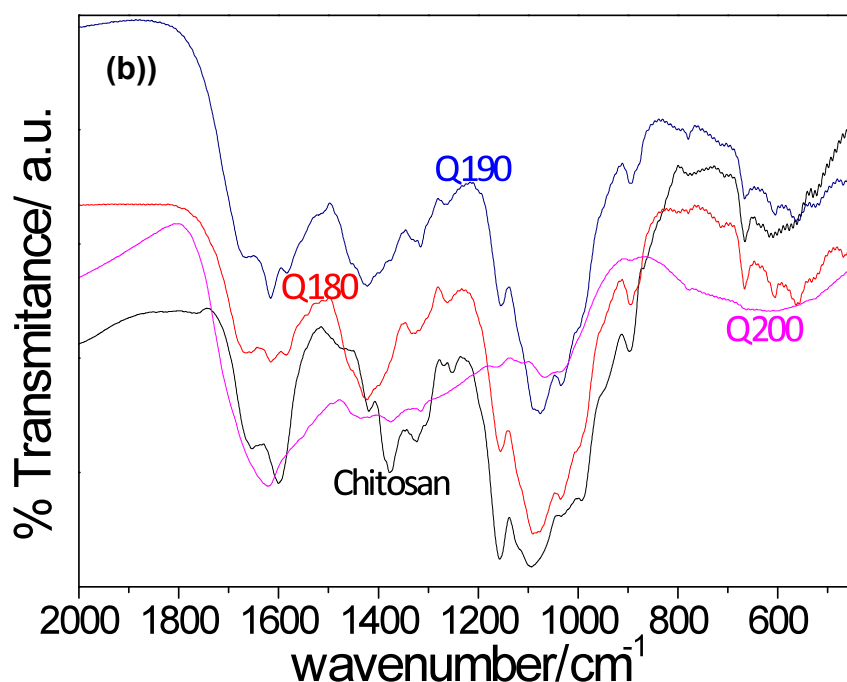
Figure 4. FTIR spectra of chitosan and representative samples of the hydrothermal carbons, (a) from 4500cm^{-1} to 2000cm^{-1}, (b) from 2000cm^{-1} to 400cm^{-1}.

The nitrogen adsorption isotherms at 77K for the HTC samples, not shown here, can be classified as type II according to IUPAC [36], which indicates materials without any significant development of the pore structure Some results recently published by Titirici and co-workers, with CO_2 adsorption at 0ºC, showed limited pore volumes and apparent specific surface areas for samples hydrothermally treated at 180ºC for 24h, with pore volume between 0.63-0.07cm^{3}g^{-1} and surface areas between 173-224m^{2}g^{-1} [31].

3.2. Characterization of activated carbons

As shown in Fig. 5, the activated carbons have lost almost all sphere-like structures visible on the HTC morphology. The morphology of the activated carbon samples is dependent of the activation method used, it can be seen that the carbon dioxide activation leads to layered carbon materials with a structure similar to the lignocelulosic materials. It is also interesting to observe the formation of nanofilaments and the preservation of some sphere-like particles on the sample ACa-5, produced by activation with $CaCO_3$.
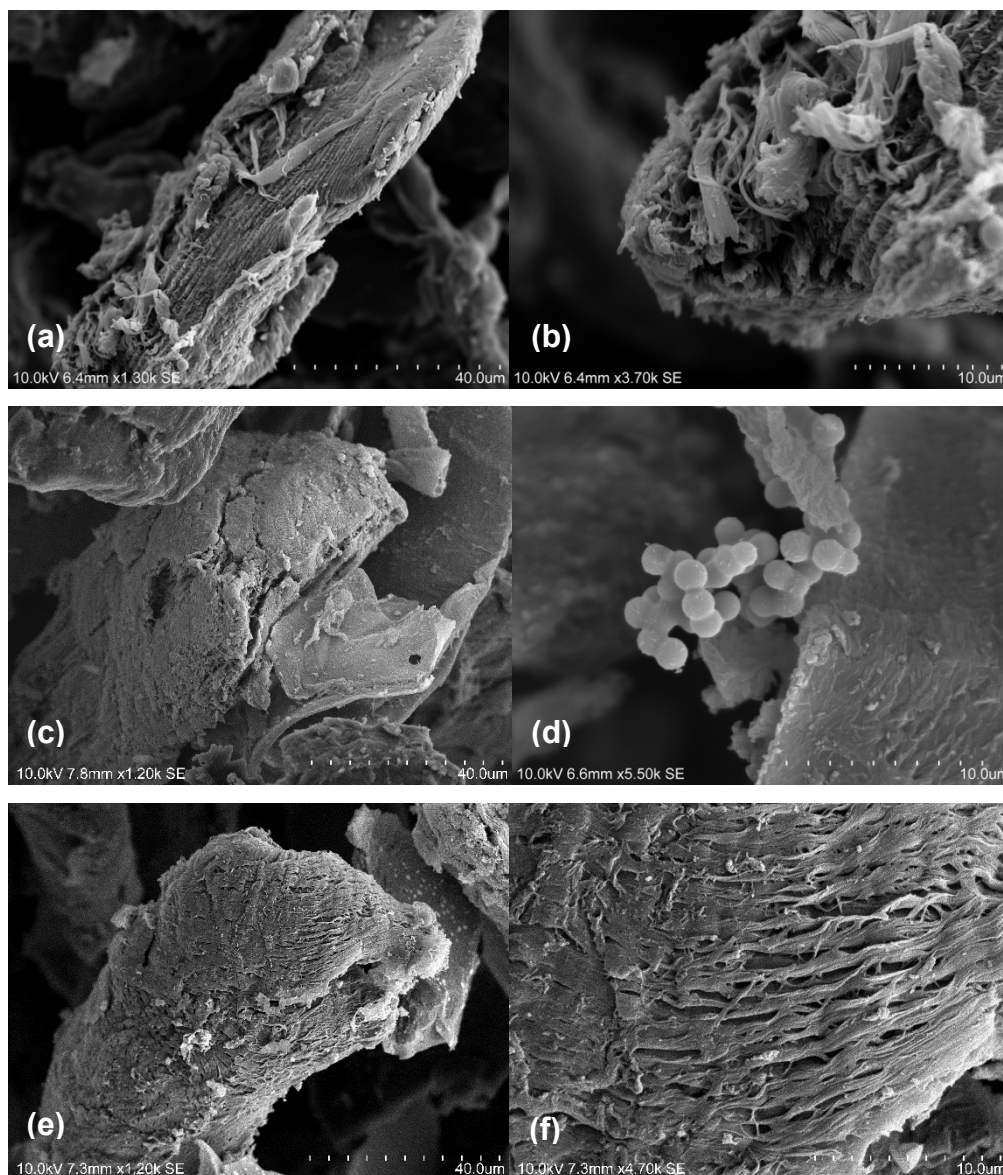
Figure 5. SEM images of activated samples AC-3 ((a) and (b)), ACa-5 ((c) and (d)) and AK-1 ((e) and (f)).

The nitrogen adsorption/desorption isotherms at 77K are shown in Fig. 6. All isotherms can be classified as type I, according to IUPAC [36], which are characteristic of materials with a well-developed pore system with predominance of micropores. The isotherms are reversible, without the presence of a hysteresis cycle, with a well-defined plateau parallel to the horizontal axis. The exception is sample ACa-5 that does not exhibit such a plateau.

The porous properties of the activated carbon samples, shown in Table 3, were determined by the analysis of the nitrogen isotherms using suitable methods, namely Brunnauer-Emmett-Teller (BET), Dubinin-Radushkevich (DR), density functional

theory (DFT) and α_s method. The volume of micropores, V_{mic}, corresponds to the volume adsorbed at p/p°=0.1 and the volume of mesopores, V_{mes}, estimated as the difference between the volume of nitrogen adsorbed at p/p°=0.95 and p/p°=0.1. The apparent specific surface area was calculated by the BET method from the adsorption data obtained in the relative pressure (p/p°) range of 0.04 to 0.2. The pore size distribution (PSD) was calculated via a non-local density functional theory (NLDFT) method assuming a slit pore model. The volume of the primary micropores (<0.7 nm) was determined by applying the Dubinin–Radushkevitch (D–R) equation.

As expected from the isotherms' shape, all samples are predominantly microporous with a low volume of mesopores. The samples produced via activation with K_2CO_3 and sample ACa-5 shows the highest mesopore volume of all samples. This sample is also the material with the highest external area, A_{ext}, 222m^{2}g^{-1}. It is also visible that the chemical activation has produced samples with a higher surface area and pore volume than samples produced by carbon dioxide activation, in particular samples produced via activation with K_2CO_3. The similarity between V_s, V_o and V_{mic} for all samples indicates that the porous structure is mainly composed by primary micropores. It is interesting to see the minimal impact of the oxidation onto the porosity of the sample AC-5. The pore volume given by the DFT method is in accordance with the volume estimated by other methods, as can be seen in Table 3.
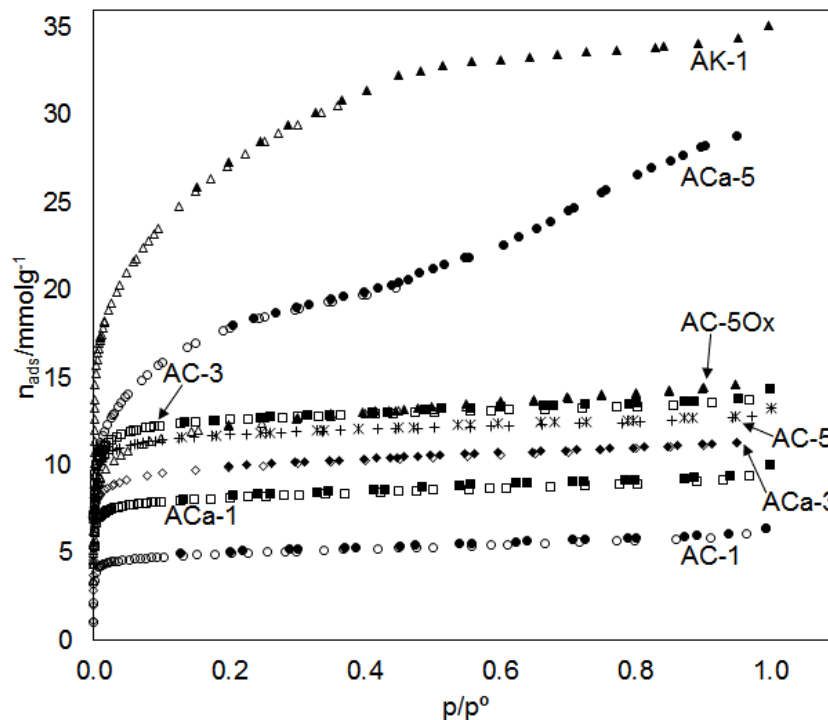

Figure 6. Nitrogen adsorption/desorption isotherms at 77K.

Table 3. Textural properties of activated carbons.

Sample	BET	α_s		DR			DFT	
	S_{BET}	V_s	A_{ext}	V_0	V_{mic}	V_{meso}	D_p	V_{pore}
	$/m^2g^{-1}$	$/cm^3g^{-1}$	$/m^2g^{-1}$	$/cm^3g^{-1}$	$/cm^3g^{-1}$	$/cm^3g^{-1}$	$/nm$	$/cm^3g^{-1}$
AC-1	423	0.18	24	0.17	0.17	0.06	1.18	0.19
AC-3	1095	0.44	21	0.42	0.43	0.07	0.86	0.44
AC-5	1023	0.41	18	0.39	0.40	0.07	0.82	0.41
ACa-1	642	0.29	19	0.28	0.27	0.07	1.13	0.30
ACa-3	852	0.36	22	0.34	0.33	0.06	0.87	0.32
ACa-5	1432	0.69	222	0.54	0.55	0.45	0.95	0.67
AK-1	2130	1.12	45	0.92	0.82	0.40	1.18	1.08
AC-5Ox	1034	0.46	36	0.38	0.40	0.10	0.89	0.46

Figure 7 shows the pore size distribution estimated by DFT. It can be seen that all samples present a narrow pore size distribution with the exception of the samples produced by activation with K_2CO_3. The results obtained for the total pore volume from DFT calculations are in good agreement with the ones obtained by the alpha-s method; This resemblance shows the applicability of DFT method in microporous activated carbons specially when applied to low relative pressures.
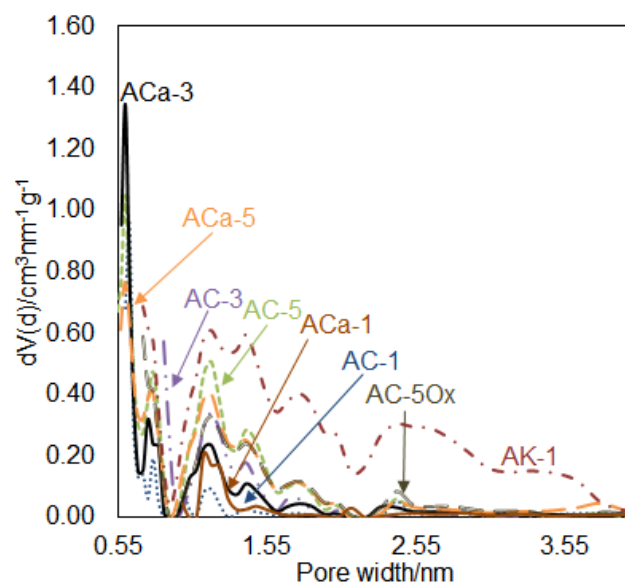
Figure 7. Pore size distribution calculated using NLDFT equilibrium model with a slit pore system.

The elemental analysis of the activated carbon samples showed a carbon content between 76 and 85%(w/w), after the oxidation process the carbon content have decreased to 44%(w/w). Regarding the nitrogen content we can observe that samples show an interesting value, between 3 to 6%(w/w), which is slightly lower than in HTC samples but indicates the retention of nitrogen within the structure of the material. The sample activated with K_2CO_3 showed lower nitrogen content, possibly as a result of the activation process. The oxygen content was around 10%(w/w) for all samples except for the sample AC-5Ox that, as expected, showed a much higher content approximately 24%(w/w). The increase in oxygen content is matching well with the point of zero charge, around 2.54 for the oxidized sample and 8.77 for AC-5. All non-oxidized samples are of basic nature with point of zero charge around 9.

Table 4. Elemental analysis and point of zero charge of activated samples.

Sample	pcz	Elemental Analysis / %(w/w)				
		C	N	H	S	O
AC-1	9.34	75.94	5.80	1.23	<d.l.	8.73
AC-3	8.76	83.20	5.23	0.25	<d.l.	10.69
AC-5	8.77	81.08	5.93	1.00	<d.l.	11.92
ACa-1	a)	80.06	5.92	0.87	<d.l.	9.13
ACa-3	a)	81.13	5.25	1.04	<d.l.	10.47
ACa-5	a)	85.32	5.45	0.93	<d.l.	12.85
AC-5Ox	2.54	44.02	3.22	0.77	<d.l.	23.92
AK-1	a)	69.87	1.19	0.89	<d.l.	a)

a) not determined; d.l. – detection limit

The FTIR spectra of the activated carbons are shown in Figure 8. The wide band between 3430-3450cm^{-1} can be attributed to OH stretching vibration or NH stretching vibration revealing the presence of amine groups. Moreover the peak at 1085-1100cm^{-1} and 1560-1616cm^{-1} can be attributed to C-N stretching vibrations and N-H bending, respectively, which supports the presence of primary and secondary amine groups. Additionally the band at 1280cm^{-1} may be related to C-N stretching vibration and the band at 779-800cm^{-1} to NH wagging vibration. The bands at 2925-2950cm-1 and 2855-2880cm-1 related to symmetric and antisymmetric stretching vibration of CH bond, respectively, indicate the presence of aliphatic groups. The materials show the presence of alcohol groups, as supported by the presence of its characteristic vibrational modes such as deformation of OH bond, at 1400cm^{-1} and 1280cm^{-1}, stretching of C-O bond at 1090-1157cm^{-1} as well as at 1065cm^{-1}. The oxidized sample shows the presence of carbonyl groups, related to the presence of carboxyl acid and esters groups, supported by the band at 1716cm^{-1} related to stretching of C=O bond.
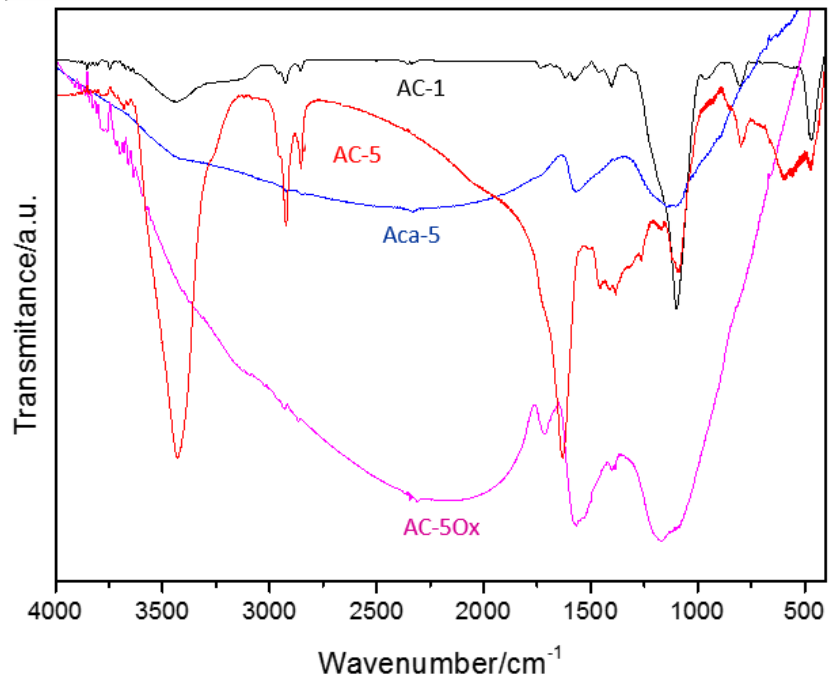
Figure 8. FTIR spectra of activated carbons.

4. Conclusions

In this work we report the successful preparation of activated carbons from chitosan via a procedure that uses a combination of hydrothermal carbonization with activation methods. The optimal carbonization conditions are 200ºC for 24h using a water:precursor ratio of 1:6. The hydrocarbons are all slightly acidic with the point of zero charge 5.9±0.2 and with very low porosity. Sample Q200-24, prepared under the conditions above described, was activated with CO_2, $CaCO_3$ and K_2CO_3 to produce activated carbon samples. The activated carbons prepared from chitosan present significant nitrogen content of 5.23 to 5.93%(w/w) without any post-production treatment, which is an advantage over other methods. The exception is the sample activated with K_2CO_3 that shows a lower value. The oxidation with nitric acid lead to a decrease of the nitrogen content and also of the point of zero charge but not the porosity. The activated carbons are all predominantly microporous with BET surface area between 400 and $2130 m^2 g^{-1}$ and a pore volume between 0,18 and $1,12 cm^3 g^{-1}$.

References

[1] H.W. Kroto, J.R. Heath, S.C. O'Brien, R.F. Curl, R.E. Smalley, C60: Buckminsterfullerene, Nature, 318 (1985) 162-163.
[2] S. Iijima, Helical microtubules of graphitic carbon, Nature, 354 (1991) 56-58.
[3] W. Hao, E. Björkman, M. Lilliestråle, N. Hedin, Activated carbons prepared from hydrothermally carbonized waste biomass used as adsorbents for CO2, Applied Energy, 112 (2013) 526-532.
[4] S. Babel, T.A. Kurniawan, Low-cost adsorbents for heavy metals uptake from contaminated water: a review, Journal of hazardous materials, 97 (2003) 219-243.
[5] P. Mourão, C. Laginhas, F. Custódio, J.V. Nabais, P. Carrott, M.R. Carrott, Influence of oxidation process on the adsorption capacity of activated carbons from lignocellulosic precursors, Fuel Processing Technology, 92 (2011) 241-246.
[6] J.V. Nabais, J. Gomes, P. Carrott, C. Laginhas, S. Roman, Phenol removal onto novel activated carbons made from lignocellulosic precursors: Influence of surface properties, Journal of hazardous materials, 167 (2009) 904-910.
[7] J.V. Nabais, A. Mouquinho, C. Galacho, P. Carrott, M.R. Carrott, In vitro adsorption study of fluoxetine in activated carbons and activated carbon fibres, Fuel Processing Technology, 89 (2008) 549-555.

[8] A.C. Dillon, K.M. Jones, T.A. Bekkedahl, C.H. Kiang, D.S. Bethune, M.J. Heben, Storage of hydrogen in single-walled carbon nanotubes, Nature, 386 (1997) 377-379.

[9] D. Cao, Y. Sun, G. Wang, Direct carbon fuel cell: fundamentals and recent developments, Journal of Power Sources, 167 (2007) 250-257.

[10] S. Giddey, S. Badwal, A. Kulkarni, C. Munnings, A comprehensive review of direct carbon fuel cell technology, Progress in Energy and Combustion Science, 38 (2012) 360-399.

[11] B.R. Selvi, D. Jagadeesan, B. Suma, G. Nagashankar, M. Arif, K. Balasubramanyam, M. Eswaramoorthy, T.K. Kundu, Intrinsically fluorescent carbon nanospheres as a nuclear targeting vector: delivery of membrane-impermeable molecule to modulate gene expression in vivo, Nano letters, 8 (2008) 3182-3188.

[12] K. Ranganathan, Adsorption of Hg (II) ions from aqueous chloride solutions using powdered activated carbons, Carbon, 41 (2003) 1087-1092.

[13] M.F. Tennant, D.W. Mazyck, The role of surface acidity and pore size distribution in the adsorption of 2-methylisoborneol via powdered activated carbon, Carbon, 45 (2007) 858-864.

[14] J.J. Freeman, Active carbon Edited by R. C. Bansal, J.-B. Donnet and F. Stoeckli. Marcel Dekker, New York, 1988, pp. xiv + 482, US$150.00. ISBN 0–8247–7842–1, Journal of Chemical Technology & Biotechnology, 48 (1990) 240-241.

[15] B. Crittenden, A. Patton, C. Jouin, S. Perera, S. Tennison, J.A.B. Echevarria, Carbon monoliths: a comparison with granular materials, Adsorption, 11 (2005) 537-541.

[16] A.J. Romero-Anaya, M. Ouzzine, M. Lillo-Ródenas, A. Linares-Solano, Spherical carbons: Synthesis, characterization and activation processes, Carbon, 68 (2014) 296-307.

[17] Z. Liu, L. Ling, W. Qiao, L. Liu, Effect of hydrogen on the mesopore development of pitch-based spherical activated carbon containing iron during activation by steam, Carbon, 37 (1999) 2063-2066.

[18] W. Qin, X.-Y. Liang, R. Zhang, C.-J. Liu, X.-J. Liu, W.-M. Qiao, Z. Liang, L.-c. LING, Preparation of polystyrene-based activated carbon spheres and their adsorption of dibenzothiophene, New Carbon Materials, 24 (2009) 55-60.

[19] A. Demirbas, Biodiesel from waste cooking oil via base-catalytic and supercritical methanol transesterification, Energy Conversion and Management, 50 (2009) 923-927.

[20] S.M. Heilmann, L.R. Jader, L.A. Harned, M.J. Sadowsky, F.J. Schendel, P.A. Lefebvre, M.G. Von Keitz, K.J. Valentas, Hydrothermal carbonization of microalgae II. Fatty acid, char, and algal nutrient products, Applied Energy, 88 (2011) 3286-3290.

[21] S.M. Heilmann, L.R. Jader, M.J. Sadowsky, F.J. Schendel, M.G. Von Keitz, K.J. Valentas, Hydrothermal carbonization of distiller's grains, biomass and bioenergy, 35 (2011) 2526-2533.

[22] S. Xiu, A. Shahbazi, V. Shirley, D. Cheng, Hydrothermal pyrolysis of swine manure to bio-oil: effects of operating parameters on products yield and characterization of bio-oil, Journal of analytical and applied pyrolysis, 88 (2010) 73-79.

[23] X. Liang, M. Zeng, C. Qi, One-step synthesis of carbon functionalized with sulfonic acid groups using hydrothermal carbonization, Carbon, 48 (2010) 1844-1848.

[24] H. Dai, Carbon nanotubes: synthesis, integration, and properties, Accounts of chemical research, 35 (2002) 1035-1044.

[25] M.-M. Titirici, A. Funke, A. Kruse, Chapter 12 - Hydrothermal Carbonization of Biomass, in: A.P.B.S.K. Sukumaran (Ed.) Recent Advances in Thermo-Chemical Conversion of Biomass, Elsevier, Boston, 2015, pp. 325-352.

[26] J.M.V.N. P.J.M. Carrott, M.M.L. Ribeiro Carrott, J.A. Menendez, Thermal treatments of activated carbon fibres using a microwave furnace, Microporous and Mesoporous Materials, 47 (2001) 10.

[27] J.M.V. Nabais, P. Nunes, P.J. Carrott, M.M.L.R. Carrott, A.M. García, M. Díaz-Díez, Production of activated carbons from coffee endocarp by CO 2 and steam activation, Fuel Processing Technology, 89 (2008) 262-268.

[28] J.V. Nabais, C. Laginhas, M.R. Carrott, P. Carrott, J.C. Amorós, A.N. Gisbert, Surface and porous characterisation of activated carbons made from a novel biomass precursor, the esparto grass, Applied surface science, 265 (2013) 919-924.

[29] J.V. Nabais, C. Laginhas, P. Carrott, M.R. Carrott, Thermal conversion of a novel biomass agricultural residue (vine shoots) into activated carbon using activation with CO 2, Journal of Analytical and Applied Pyrolysis, 87 (2010) 8-13.

[30] L. Yu, C. Falco, J. Weber, R.J. White, J.Y. Howe, M.-M. Titirici, Carbohydrate-derived hydrothermal carbons: a thorough characterization study, Langmuir, 28 (2012) 12373-12383.

[31] C. Falco, N. Baccile, M.-M. Titirici, Morphological and structural differences between glucose, cellulose and lignocellulosic biomass derived hydrothermal carbons, Green Chemistry, 13 (2011) 3273-3281.

[32] C. Falco, F. Perez Caballero, F. Babonneau, C. Gervais, G. Laurent, M.-M. Titirici, N. Baccile, Hydrothermal carbon from biomass: structural differences between hydrothermal and pyrolyzed carbons via 13C solid state NMR, Langmuir, 27 (2011) 14460-14471.

[33] S. Román, J. Nabais, C. Laginhas, B. Ledesma, J. González, Hydrothermal carbonization as an effective way of densifying the energy content of biomass, Fuel Processing Technology, 103 (2012) 78-83.

[34] S. Roman, J.V. Nabais, B. Ledesma, J. González, C. Laginhas, M. Titirici, Production of low-cost adsorbents with tunable surface chemistry by conjunction of hydrothermal carbonization and activation processes, Microporous and Mesoporous Materials, 165 (2013) 127-133.

[35] M. Sevilla, J.A. Maciá-Agulló, A.B. Fuertes, Hydrothermal carbonization of biomass as a route for the sequestration of CO 2: chemical and structural properties of the carbonized products, Biomass and Bioenergy, 35 (2011) 3152-3159.

[36] K.S. Sing, Reporting physisorption data for gas/solid systems with special reference to the determination of surface area and porosity (Recommendations 1984), Pure and applied chemistry, 57 (1985) 603-619.

Tables

Table 1. Elemental analysis of the precursor

Precursor	Elemental Analysis / %(w/w)					
	C	N	H	S	O	Undetermined[a]
Chitosan	40.38	7.72	7.81	<d.l.	33.70	10.39

a - by difference; d.l. – detection limit

Table 2. Elemental analysis and point of zero charge of the hydrothermal carbons

Sample	pH_{pzc}	Elemental Analysis / %(w/w)				Undetermined (%w/w)[a]
		C	N	H	O	
Q180-8	5.77	40.93	7.68	16.38	28.02	6.99
Q180-12	5.81	42.00	7.66	15.89	27.24	7.21
Q180-24	5.82	45.15	8.21	9.95	27.05	9.64
Q190-8	5.79	37.46	7.70	14.81	29.50	10.53
Q190-12	5.85	43.58	7.80	13.36	25.76	9.50
Q190-24	5.98	55.11	9.41	8.68	21.47	5.33
Q200-8	5.85	48.65	8.28	12.37	25.05	5.65
Q200-12	5.89	54.67	9.19	10.96	19.08	6.10
Q200-24	6.01	59.62	10.07	4.97	16.42	8.92

a) by difference

Table 3. Textural properties of activated carbons.

Sample	BET	α_s		DR			DFT	
	S_{BET} /m^{2}g^{-1}	V_s /cm^{3}g^{-1}	A_{ext} /m^{2}g^{-1}	V_0 /cm^{3}g^{-1}	V_{mic} /cm^{3}g^{-1}	V_{meso} /cm^{3}g^{-1}	D_p /nm	V_{pore} /cm^{3}g^{-1}
AC-1	423	0.18	24	0.17	0.17	0.06	1.18	0.19
AC-3	1095	0.44	21	0.42	0.43	0.07	0.86	0.44
AC-5	1023	0.41	18	0.39	0.40	0.07	0.82	0.41
ACa-1	642	0.29	19	0.28	0.27	0.07	1.13	0.30
ACa-3	852	0.36	22	0.34	0.33	0.06	0.87	0.32
ACa-5	1432	0.69	222	0.54	0.55	0.45	0.95	0.67
AK-1	2130	1.12	45	0.92	0.82	0.40	1.18	1.08
AC-5Ox	1034	0.46	36	0.38	0.40	0.10	0.89	0.46

Table 4. Elemental analysis and point of zero charge of activated samples.

Sample	pcz	Elemental Analysis / %(w/w)				
		C	N	H	S	O
AC-1	9.34	75.94	5.80	1.23	<d.l.	8.73
AC-3	8.76	83.20	5.23	0.25	<d.l.	10.69
AC-5	8.77	81.08	5.93	1.00	<d.l.	11.92
ACa-1	a)	80.06	5.92	0.87	<d.l.	9.13
ACa-3	a)	81.13	5.25	1.04	<d.l.	10.47
ACa-5	a)	85.32	5.45	0.93	<d.l.	12.85
AC-5Ox	2.54	44.02	3.22	0.77	<d.l.	23.92
AK-1	a)	69.87	1.19	0.89	<d.l.	a)

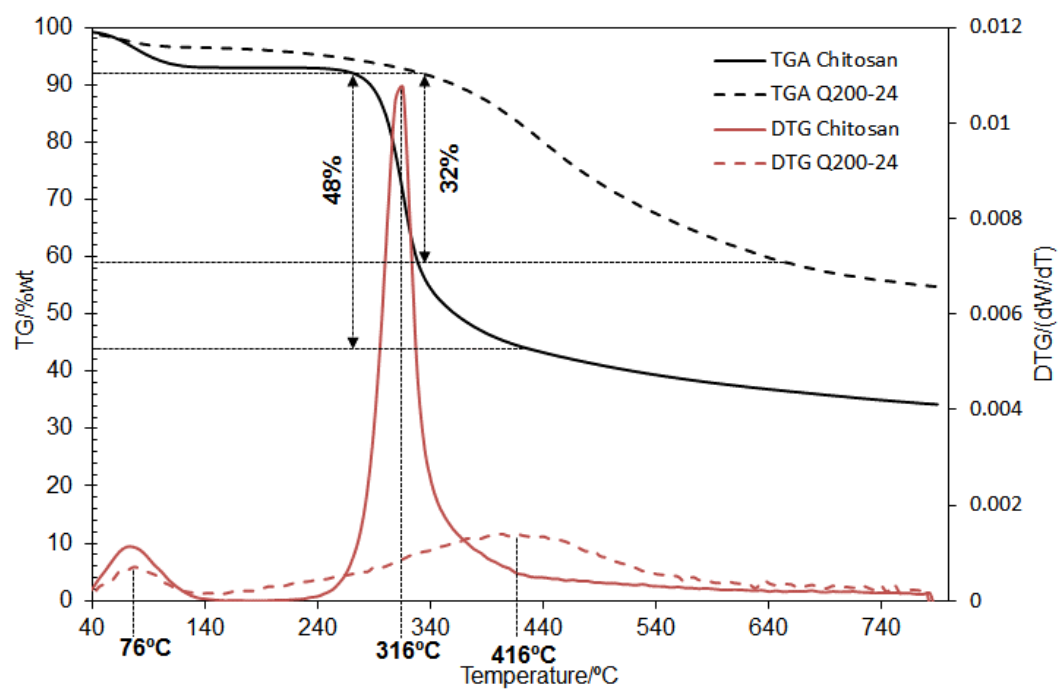a) not determined; d.l. – detection limit

Figures captions

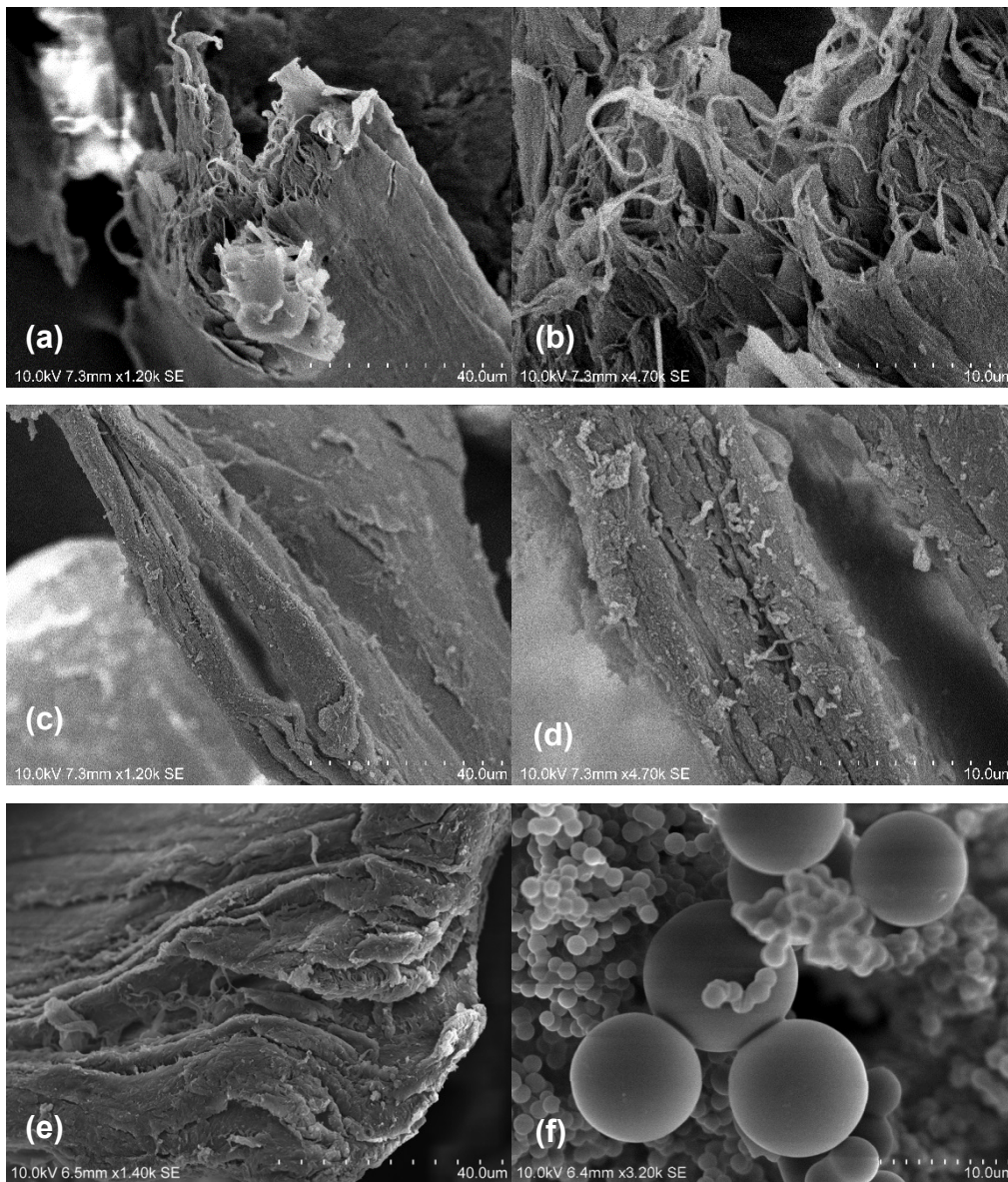Figure 1. TGA and DTG curves of chitosan and Q200-24

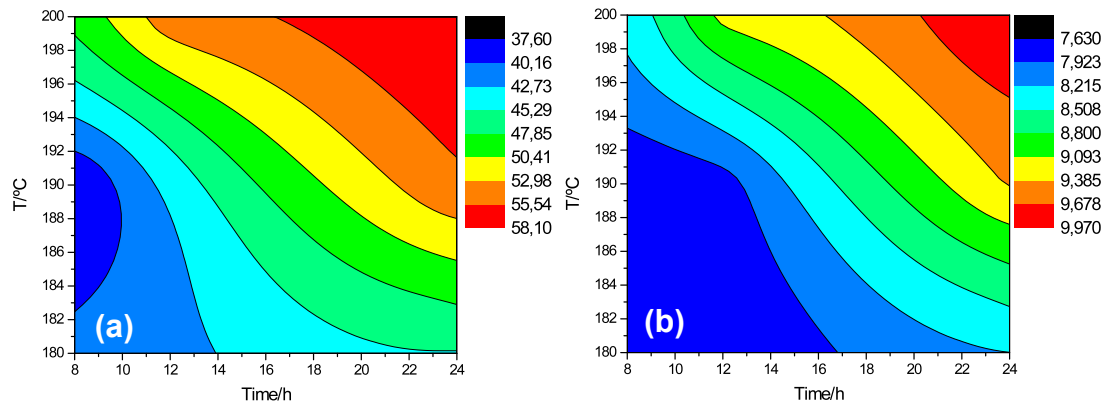Figure 2. SEM images of Q200-8 ((a) and (b)), Q200-12 ((c) and (d)) and Q200-24 ((e) and (f)).

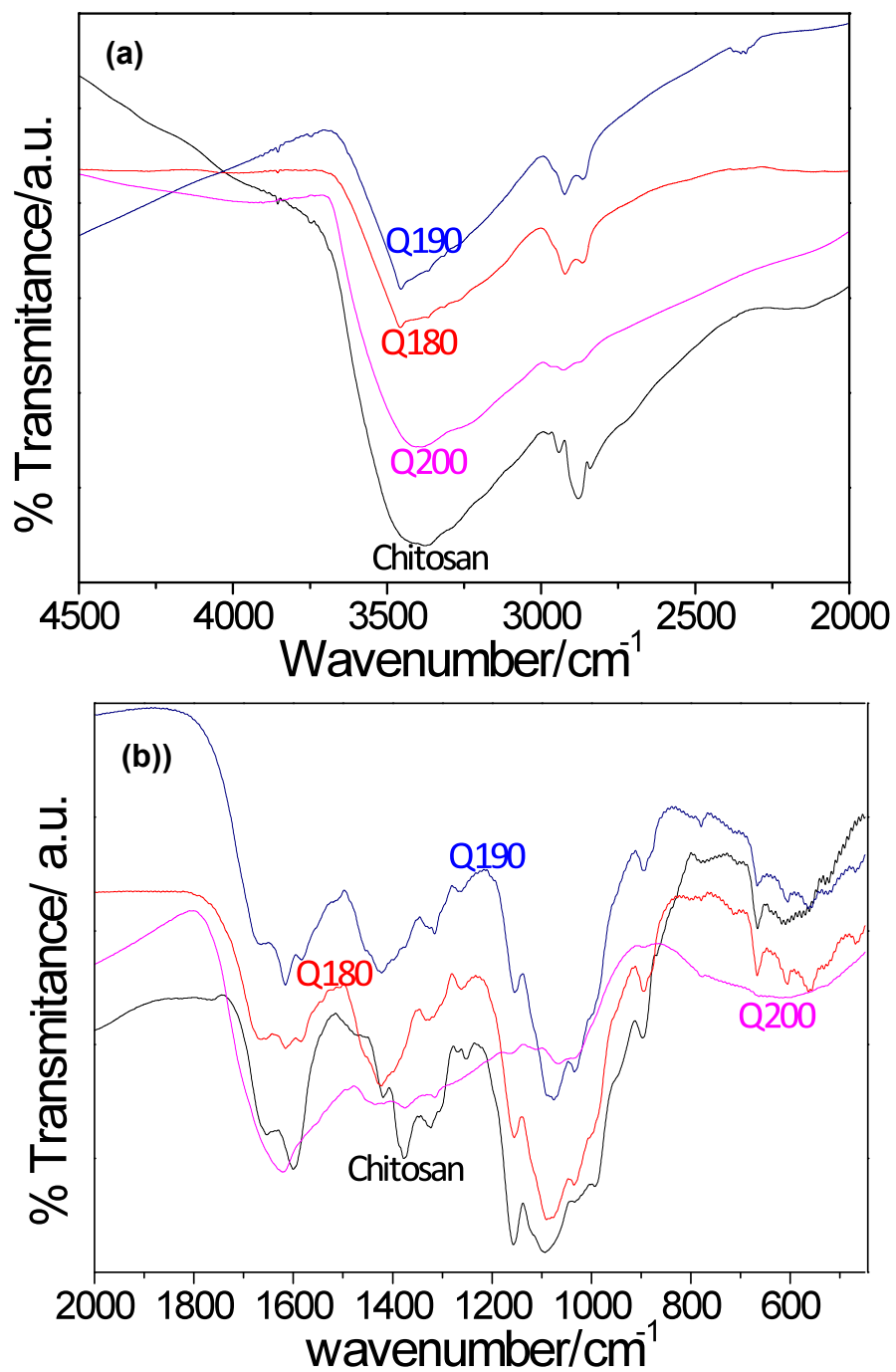Figure 3. Carbon (a) and nitrogen (b) content in HTC samples.

Figure 4. FTIR spectra of chitosan and representative samples of the hydrothermal carbons, (a) from $4500cm^{-1}$ to $2000cm^{-1}$, (b) from $2000cm^{-1}$ to $400cm^{-1}$.
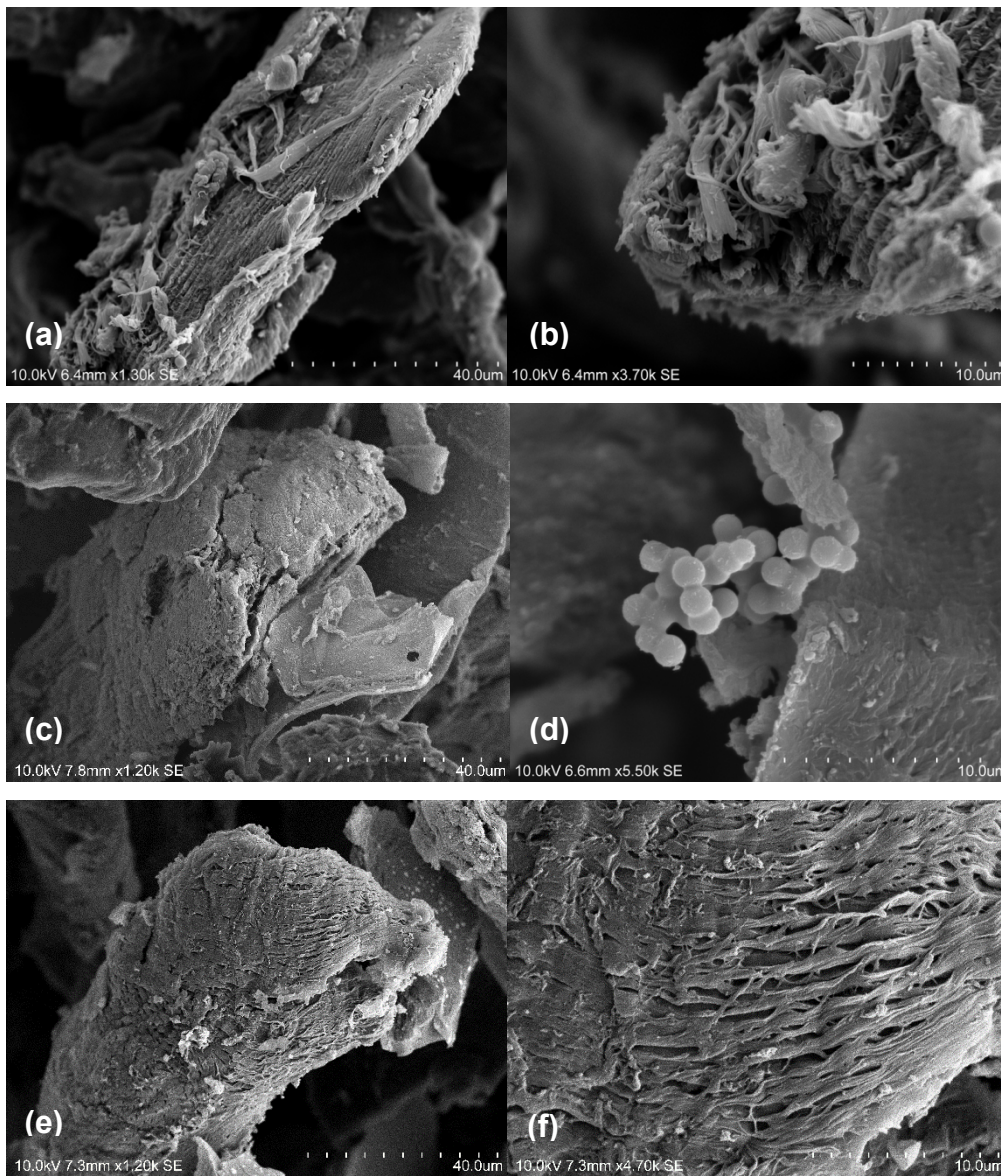
Figure 5. SEM images of activated samples AC-3 ((a) and (b)), ACa-5 ((c) and (d)) and AK-1 ((e) and (f)).
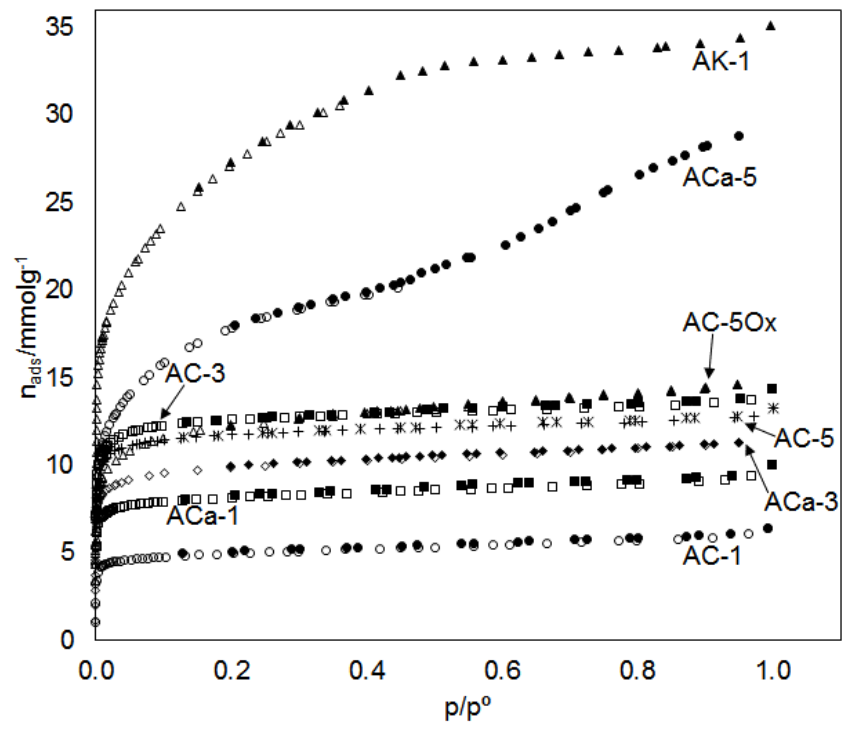
Figure 6. Nitrogen adsorption/desorption isotherms at 77K.

Figure 7. Pore size distribution calculated using NLDFT equilibrium model with a slit pore system.

Figure 8. FTIR spectra of activated carbons.

Figures

Figure 1. TGA and DTG curves of chitosan and Q200-24

Figure 2. SEM images of Q200-8 ((a) and (b)), Q200-12 ((c) and (d)) and Q200-24 ((e) and (f)).

Figure 3. Carbon (a) and nitrogen (b) content in HTC samples.

Figure 4. FTIR spectra of chitosan and representative samples of the hydrothermal carbons, (a) from 4500cm⁻¹ to 2000cm⁻¹, (b) from 2000cm⁻¹ to 400cm⁻¹.

Figure 5. SEM images of activated samples AC-3 ((a) and (b)), ACa-5 ((c) and (d)) and AK-1 ((e) and (f)).

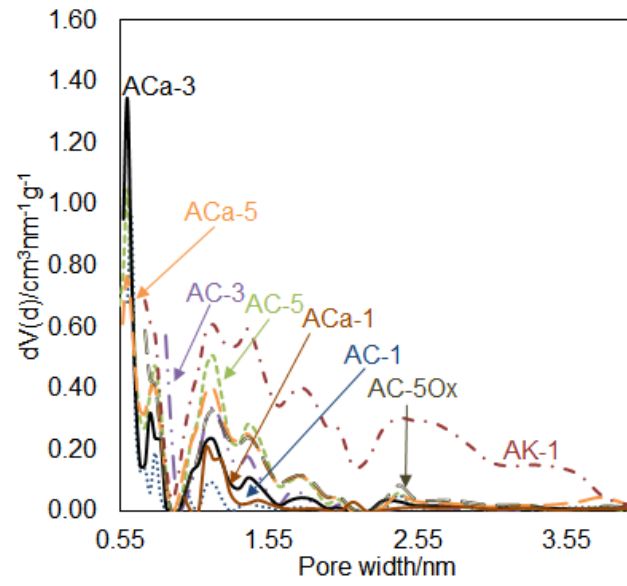Figure 6. Nitrogen adsorption/desorption isotherms at 77K.

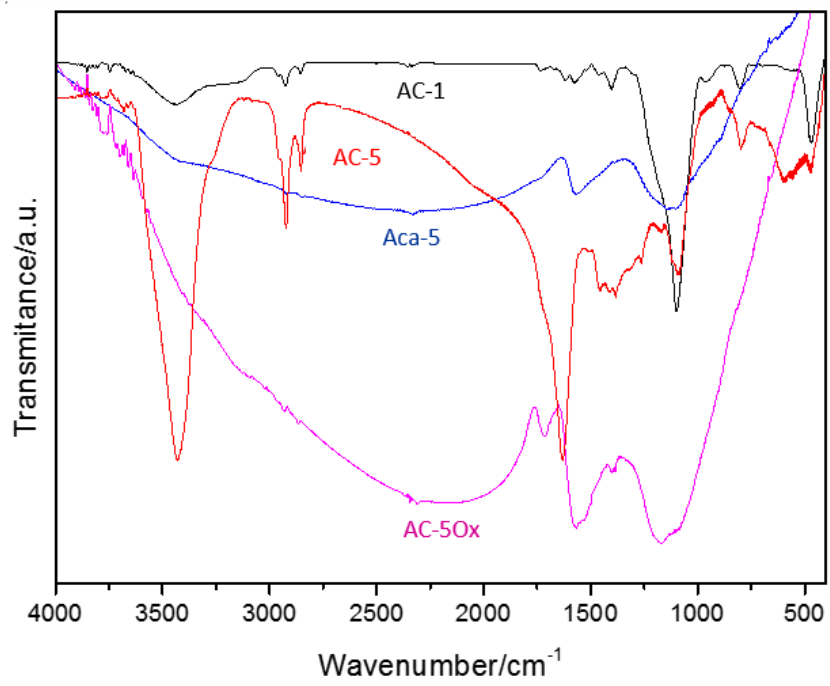Figure 7. Pore size distribution calculated using NLDFT equilibrium model with a slit pore system.

Figure 8. FTIR spectra of activated carbons.